On the influence of cross-sectional deformations on the aerodynamic performance of wind turbine rotor blades

Julia Gebauer[1], Felix Prigge[1], Dominik Ahrens[2], Lars Wein[2], and Claudio Balzani[1]

[1]Institute for Wind Energy Systems, Leibniz University Hannover, Appelstr. 9A, 30167 Hanover, Germany
[2]Institute of Turbomachinery and Fluid Dynamics, Leibniz University Hannover, An der Universität 1, 30823 Garbsen, Germany

Correspondence: Julia Gebauer (research@iwes.uni-hannover.de)

Abstract. The aerodynamic performance of a wind turbine rotor blade depends on the geometry of the used airfoils. The airfoil shape can be affected by elastic deformations of the blade during operation due to structural loads. This paper provides an initial estimation of the extent to which cross-sectional deformations influence the aerodynamic load distribution along the rotor blade. The IEA 15 MW reference wind turbine model is used for this study. A constant wind field at the rated wind speed is applied as an operational load test case. The resulting loads are calculated by an aero-servo-elastic simulation of the turbine. The loads are applied to a 3D finite shell element (FE) model of the rotor blade, which serves to calculate the cross-sectional deformations. For the individual cross-sections in the deformed configuration, the new lift and drag coefficients are calculated. These are then included in the aero-servo-elastic simulation and the obtained results are compared with those of the initial simulation that is based on the undeformed cross-sections. The cross-sectional deformations consist of a change in the chord length and the geometry of the trailing edge panels and depend on the azimuth position of the blade. The change in the airfoil geometries results in altered aerodynamic characteristics and therefore in a deviation of the blade root bending moments, the maximum change of which is -1.4% in the in-plane direction and +0.71% in the out-of-plane direction. Although these values are relatively small, the initial results imply that further investigations should be carried out with more complex wind fields and different rotor blade designs to identify aero-structural couplings that could potentially be critical for the design of rotor blades or other wind turbine components.

1 Introduction

The rotor blade is a crucial element in the generation of electrical power from wind in modern wind turbines. The blades are exposed to a wide range of loads during their life time, which are a combination of aerodynamic, gravitational, inertial, transient, and gyroscopic loads (Hau, 2013; Söker, 2013; Liu et al., 2017; Burton et al., 2021). Especially the wind inflow and the blade mass contribute significantly to out-of-plane and in-plane bending moments.

The amount of energy that can be extracted from the wind depends on the aerodynamic design of the rotor blade, i. e., the shape of the outer shell. The aerodynamic design is a sequence of airfoils that are threaded along the blade axis. A high lift-to-drag ratio in each individual airfoil is desirable for maximum power generation. The

geometry of the airfoil and the angle of attack, which depends on the aerodynamic twist angle, are crucial for a high aerodynamic performance. However, a high power output is normally accompanied by high aerodynamic and consequentially high mechanical loads acting on the blade. Thus, a compromise must always be found in the blade design between aerodynamic and structural performance (Hansen, 2015; Bak, 2023).

The structural design of a rotor blade provides high stiffness and strength with respect to its weight. In the context of this paper, the structural design of the blade defines its resistance against cross-sectional deformations, and thus the resistance against changes of the blade geometry and the resulting aerodynamic performance. The cross-sectional stiffness depends on the choice of materials, the structural topology, and the layup of the composite structures (Schürmann et al., 2007; Vassilopoulos, 2013). With currently used materials and classical blade topologies and layups, and the tendency towards larger rotor blades, the weight, the generated power, and thus the structural loads, which are understood as the internal forces and moments in the blades and other structural members, increase. When optimising the design with the minimisation of the blade mass as an optimisation target, an increasingly elastic behaviour of the blade is expected, including the elasticity and flexibility of the cross-sections. This also means, however, that the aerodynamically designed shell, which is reinforced by the structural components of the blade, is more susceptible to changes in the overall geometry during operation.

Typically, aero-servo-elastic multibody simulation tools are utilized to design the rotor blade. Well-known tools in the market are, for instance, OpenFAST (National Renewable Energy Laboratory, 2023) and HAWC2 (**?**). While the aerodynamic module of these tools is usually based on the blade element momentum theory (**?**Jonkman et al., 2015), there are different levels of fidelity for the structural module. The HAWC2 structural model uses a Timoshenko beam embedded in a multibody formulation with the option to use a fully populated stiffness matrix (**?**). In OpenFAST one can choose between a modal reduction based on the Euler-Bernoulli beam theory (ElastoDyn, (National Renewable Energy Laboratory, 2024)) or a geometrically exact finite beam element formulation (BeamDyn, (**??**)). All these structural models have in common, that geometrically non-linear deformations at the cross-sectional level are not considered.

Ovalisations of thin-walled beam structures with circular cross-sections were described by **?**. This Brazier effect was analytically described by Cecchini and Weaver (2005) for symmetric two-bay airfoil slices.

In the meantime, blade tests revealed that cross-sectional deformations occur in rotor blades. **?** have shown experimentally and numerically that critical bending moments lead to cross-sectional deformation and thus an opening of the trailing edge. **?** conducted the fracture analysis for the trailing edge bonding of rotor blades and were able to show that in-plane deformations lead significantly to damage in the trailing edge adhesive. **?** studied the box girder experimentally and numerically. Here, the stresses in the shear webs could be measured as a result of the cross-sectional deformations. Eder and Bitsche (2015) presented an analysis of asymmetric airfoils under bi-axial bending and discussed the reduction of the fatigue life of the adhesive joints as a consequence of cross-sectional deformations. However, the aforementioned publications did not investigate the aero-elastic coupling that cross-sectional deformations may result in.

A change in geometry of the aerodynamic shell and thus the airfoils can result from various aspects. **?** investigated the change in geometry due to thermal residual stresses arising from the cool-down during manufacturing and the subsequent changes in lift and drag coefficients. They pointed out that the lift-to-drag ratios change particularly in the inboard regions of the blade. Simulations showed that the loads decreased and thus the fatigue life increased, which was accompanied by a reduction of power production. Leading edge erosion can also change the airfoil geometry due to removal of material. **?** investigated two cross-sections with different relative thicknesses in wind tunnel experiments. An increase in drag and a decrease in lift resulted in a significant decrease in overall performance. The airfoil geometry is also influenced by icing. **?** showed that the drag coefficient increases significantly, while the lift coefficient slightly decreases. Additionally, the authors compared thrust and power output for different wind speeds. They reported a shift of the power curve towards higher wind speeds, resulting in a higher rated wind speed and a lower power output in the partial load region. It can therefore be concluded that it is important to know possible cross-sectional changes and their impact on the performance of the wind turbine.

Preliminary work on the quantification of in-plane cross-sectional deformations of rotor blades due to mechanical loads was presented in (Gebauer and Balzani, 2023) and (Balzani and Gebauer, 2023). Therein, a three-dimensional finite element model was used to calculate the deformed blade shape based on the bending moment distributions from aero-servo-elastic simulations. The deformed positions of nodes associated with a cross-section of interest were projected onto a plane that was considered the cross-sectional plane in the deformed configuration, and the deformed shape of the cross-section was obtained. To the best knowledge of the authors, the impact of load-induced cross-sectional deformations on the aerodynamic behaviour of the airfoils and the coupling with the aero-elastic response of the blades was not yet investigated.

Since normal operation is the most common condition in the life of a wind turbine, the following research question arises: To what extent do cross-sectional deformations affect the aerodynamic performance of the rotor under operational conditions? A simple test case with respect to normal operation of the wind turbine and a constant wind field is selected for the initial investigation presented in this paper. The aim is to provide a first quantification of the aero-structural coupling due to cross-sectional deformations.

The content of the paper is organized in four sections. The workflow and methods are described in section 2. In section 3, the cross-sectional deformations are analysed for a reference turbine, and the changes in chord length and lift and drag coefficients are presented. The impact of the geometrical changes on the aero-elastic turbine response are examined and discussed in section 4. Section 5 draws conclusions and gives an outlook on future work.

2 Methods

The study is conducted on the model of the IEA 15 MW reference wind turbine (RWT). The rotor blades have a length of 117 m. Data of the wind turbine for load simulations and of the blades to create a three-dimensional (3D) finite element (FE) model is provided in Gaertner et al. (2020). To analyse the influence of the cross-sectional

deformations of the rotor blade on the wind turbine behaviour, a two-stage process is applied. A flow chart of the process is given in Fig. 1.

First, a 3D FE model of the rotor blade was created to obtain the 3D blade geometry. Based on the FE model geometry, the aerodynamic polars were calculated for each nodal position along the blade. The polars were fed back into the turbine simulation model and were used to calculate the aerodynamic loads via the blade element momentum theory (Jonkman et al., 2015). For the load calculation (considering aerodynamic and gravitational loading), an aero-servo-elastic simulation of the turbine was performed. The extracted loads were transformed into a global coordinate system that is used in the 3D FE simulation. With the FE model and the transformed loads, a simulation was started using an FE solver assuming clamped boundary conditions at the blade root. The deformed 2D cross-sections were then calculated from the resulting 3D blade model in the deformed configuration. For the procedure to extract the deformed cross-sections the reader is referred to Gebauer and Balzani (2023) and Balzani and Gebauer (2023). The deformed cross-sections were used to re-calculate the lift and drag coefficients. The aerodynamic polars were re-imported into the wind turbine simulation model, the aero-servo-elastic simulation was repeated and the results were analysed with respect to a change in loads and turbine behaviour. The individual steps are described in the following sections in more detail.

2.1 3D structural model of the blade

In order to determine the impact of cross-sectional deformations on the rotor aerodynamics and the wind turbine behaviour, the rotor blade must be modelled with sufficient accuracy. Moreover, the blade model must allow for the extraction of deformed shapes of the cross-sections, as this information is needed for a subsequent turbine simulation. A 3D finite shell element model was thus employed, as such model provides a reasonable compromise between accuracy and computation time. The blade model was created with the in-house Model Creation and Analysis tool MoCA that had been validated earlier using a physical full-scale blade test (Noever-Castelos et al., 2022) and had thus been proven to provide a sufficient level of accuracy. The blade model is shown in Fig. 2.

The 3D FE blade model was verified against the beam model of the reference turbine by comparing the longitudinal distributions of the chord length, the relative thickness, and the flapwise and edgewise stiffnesses. The detailed description of the verification was added to Appendix A. The relative deviation ϵ used for the verification as well as subsequent analyses is defined as follows:

$$\epsilon = \frac{x_{\mathrm{gen}} - x_{\mathrm{ref}}}{x_{\mathrm{ref}}} \, . \tag{1}$$

Herein, x_{ref} is a reference data point from the reference turbine model and x_{gen} is a data point generated by the FE model. In the following, the relative deviation is defined accordingly. The relative deviation is only evaluated at spanwise positions where data points are available for both the reference and the FE model. The FE model was used to calculate the cross-sectional deformations at a later stage of this study. The FE solver was Ansys® (2020). For a consistent comparison of the aerodynamic behaviour of the undeformed and the deformed blade and due to the

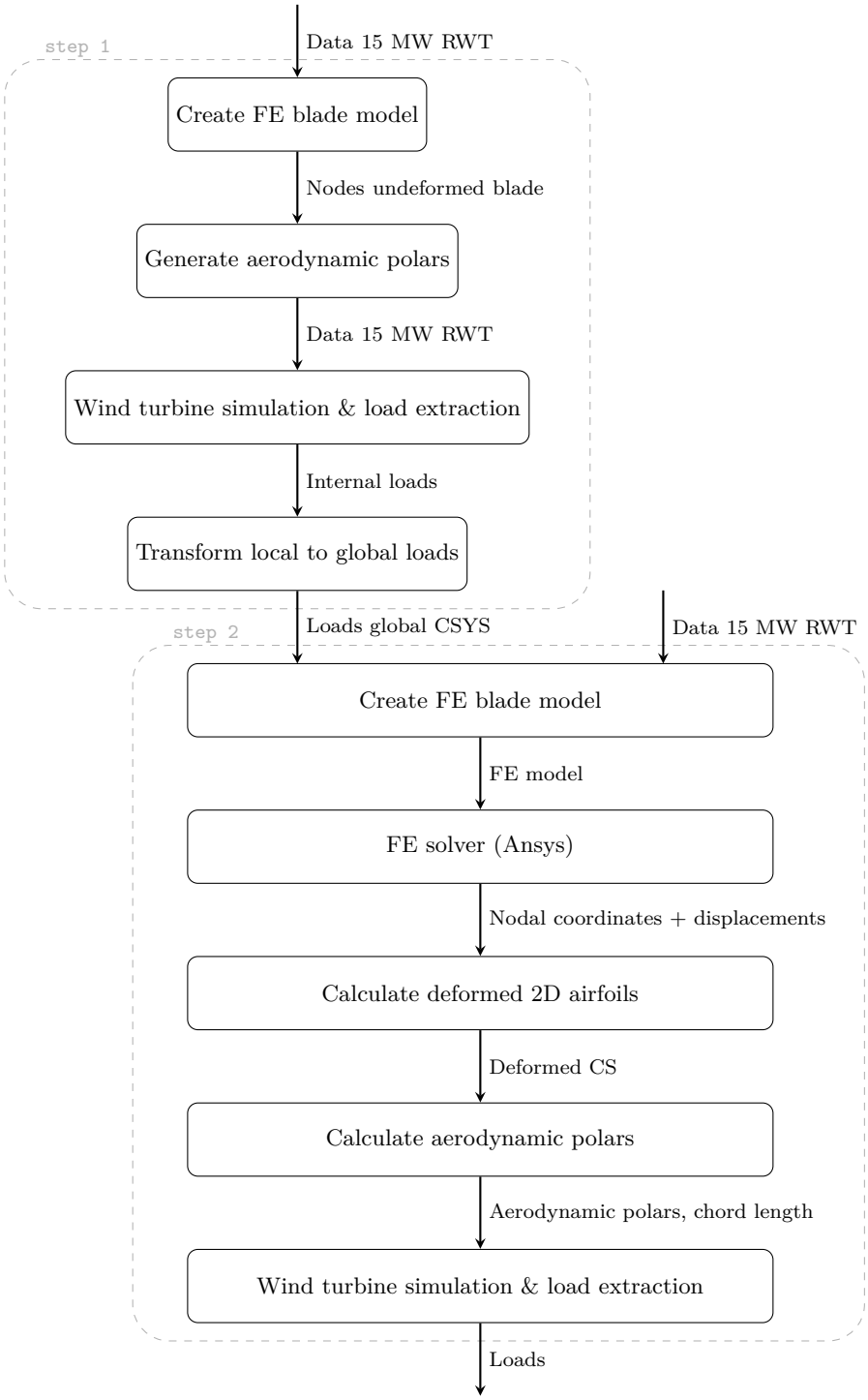

Figure 1. Flowchart of the routine to calculate the internal loads in the rotor blades taking into account cross-sectional (CS) deformations in the airfoil polars.

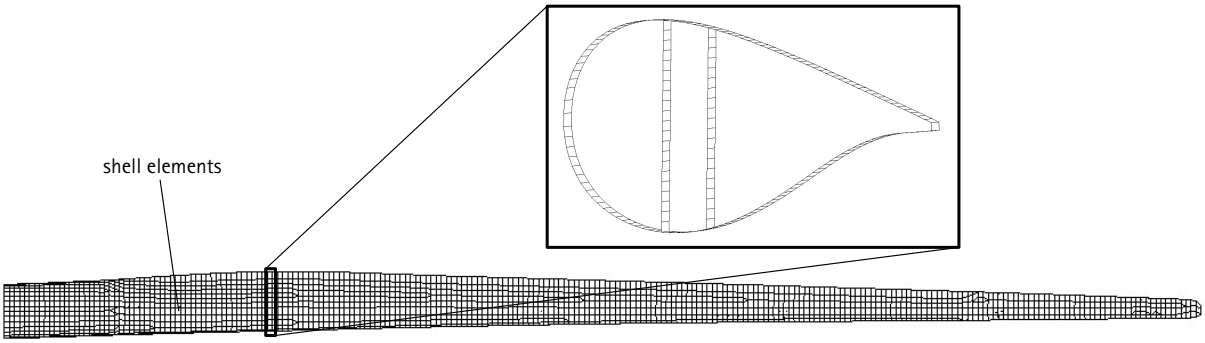

Figure 2. Finite element mesh of the 15 MW reference wind turbine blade. For visualization purposes, the blade was meshed more coarsely than in the simulations. The zoom view shows a slice of the blade model with one element in longitudinal direction at the maximum chord position.

small differences between the structural behaviour of the reference model and that of the reference model and that of the 3D FE model, the FE model was used in the following and the blade data from the reference turbine description was modified accordingly. This includes the relative thickness distribution, i. e., the aerodynamic description of the blade.

A mesh convergence study with respect to natural frequencies was carried out for the 3D FE model. The converged mesh consisted of 128,986 nodes and 131,008 quadrilateral, 4-noded shell elements with linear shape functions and 6 nodal degrees of freedom (element type SHELL181 (Ansys®, 2020)).

For the geometrically non-linear FE simulations, the rotor blade was fully clamped at the blade root. The loads were calculated via an aero-servo-elastic turbine simulation (see section 2.3). Concentrated forces in out-of-plane and in-plane direction of the rotor were applied to the 3D model at discrete locations along the blade span. The magnitude of the forces were calibrated so that the flapwise and edgewise bending moments from the loads simulations were well approximated. Applying flapwise and edgewise bending moments simultaneously results in a static and multi-axial load scenario.

The loads were applied via multi point constraints that represented a load introduction similar to load frames used in physical full-scale blade testing (IEC61400-23, 2001). As described in Noever-Castelos et al. (2022) an extra node is introduced at the load frame position. Here, the master node is defined at the shear centre of this cross-section. The substitute loads then act on the load frame position in the respective shear center, that was calculated with BECAS (Blasques and Stolpe, 2012). The loads affect the deformations in the spanwise vicinity of the load frames. According to IEC61400-23 (2001), a region corresponding to the chord length can not be taken into account in spanwise direction on both sides of the load frames (Saint-Venant principle). At the same time, the bending moment must be mapped as accurately as possible. For the positioning of the load frames the blade was divided into 50

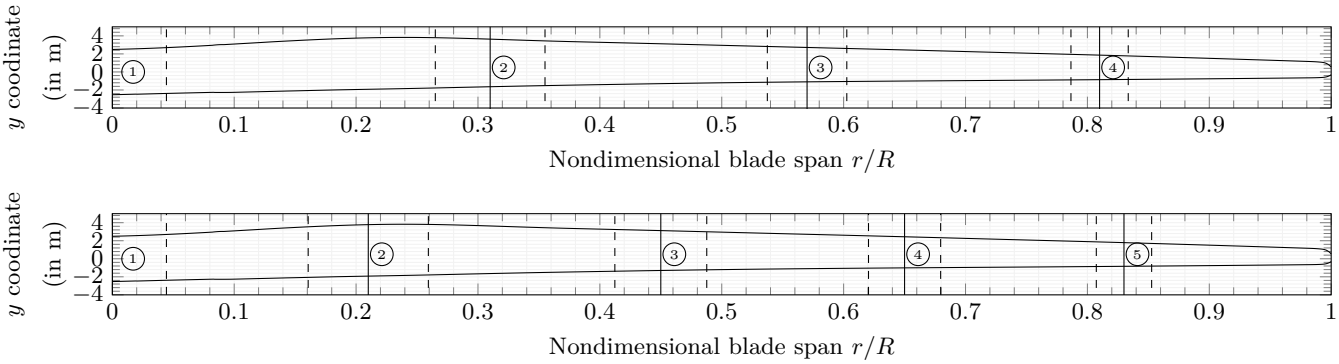

Figure 3. Load frame positions. Solid lines represent the radial load frame positions in the FE model. Dashed lines indicate the areas that cannot be evaluated.

equidistant points. An investigation was carried out for two, three, four and five load frames in which the effect of spanwise positions on the utilisable blade length and the error in bending moment were calculated. In all cases, the clamping at the blade root was considered the first load frame.

Based on the results of that investigation, five load frames were selected and positioned along the blade, see the bottom image of Fig. 3. The cross-sectional deformations were only evaluated between the load frame regions marked by dashed vertical lines. To be able to also analyse the areas around the load frames, a second set of four load frames shifted in spanwise direction were used, see the top plot of Fig. 3. Hence, for each load case two simulations were performed with four and five load frames, respectively. The outermost blade tip was not considered as a possible load frame position, as 3D FE simulations have shown that there are stability issues otherwise. That is acceptable, because the outermost region of the blade is not subjected to high mechanical loads. Hence, high cross-sectional deformations are not expected there.

2.2 Airfoil polars

For the deformed cross-sections, the airfoil polars needed to be calculated. For a consistent comparison, the polars of the undeformed cross-sections had to be calculated with the same method. The panel method implemented in XFOIL (Drela, 1989) was used for this purpose. It is known that XFOIL predicts the linear range of the lift coefficient well (Lennie et al., 2015) for thin airfoils, i. e., the results are good for small angles of attack. In the analysed operational load test case, the turbine operation mode mostly revealed angles of attack of less than 10°, which were only exceeded in the blade root area. High-fidelity computational fluid dynamics (CFD) was used to verify the polars and ensure the validity of the XFOIL results. Details for the CFD simulations are given in Appendix B.

The results of the URANS simulations are compared with the XFOIL results in Fig. 4. The lift coefficients agree very well. We can thus conclude that XFOIL can be used for the calculation of the polars along the blade. Especially in the outboard region of the blade, see on the right of Fig. 4, the XFOIL results are very accurate for an angle

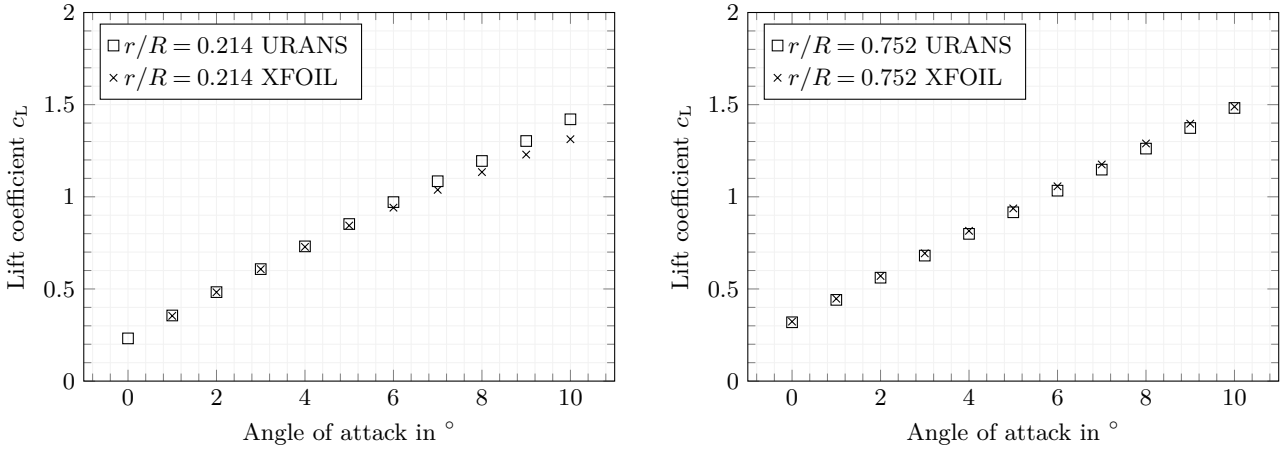

Figure 4. Lift coefficient calculated with URANS and XFOIL. The maximum sampling error is $1.84e^{-2}$ and was calculated according to Ries et al. (2018).

of attack up to 10° and almost coincide with the URANS results. For the thicker airfoils closer to the blade root, there is a slight deviation at higher angles of attack ($> 6°$) . However, since the deviation is small and due to the substantially lower computational cost, XFOIL was also used there for the analysis of the aero-elastic impact of cross-sectional deformations.

2.3 Aero-servo-elastic response of the wind turbine

Aero-servo-elastic simulations were carried out to determine the overall dynamic response of the wind turbine and to calculate the loads that the rotor blades are exposed to. The turbine simulations were carried out in two stages. The first simulation was executed to observe the behaviour of the system with undeformed cross-sections in the blade. The second simulation was carried out for deformed cross-sections, so that the dynamic behaviour of the turbine with and without cross-sectional deformations could be compared.

The aero-servo-elastic simulations were performed with OpenFAST (National Renewable Energy Laboratory, 2023). ElastoDyn (National Renewable Energy Laboratory, 2024) was used to model the structural dynamics of the blades. Therein, an Euler-Bernoulli beam theory in combination with a modal reduction is employed, where the first two flap- and the first edgewise bending modes are considered. In this study, torsion loads were neglected in the 3D model under the assumption that cross-sectional deformations are bending-dominated (recall **?**).

To focus on the influence of the cross-sectional deformations on the aero-elastic behavior of the turbine, a constant wind field at rated wind speed of 10.5 m/s was chosen in this investigation. At this wind speed the rotor experiences the highest thrust force. Moreover, this is the point at which the rotor blade is not yet pitched, so that flap- and edgewise directions coincide with the out-of-plane and in-plane directions with respect to the rotor plane.

The duration of the aero-servo-elastic simulation was 700 s. From this time span the first 100 s were removed as transient period. The remaining 600 s were used for the analysis. A full periodic rotation of one rotor blade was analysed, and the blade positions with an azimuth angle $\beta \in \{0°, 90°, 180°, 270°\}$ were the basis for the subsequent investigations, see also the blade highlighted in blue in Fig. 5. A simulation was carried out to extract the reference loads along the blade for the aforementioned azimuth positions. The flapwise and edgewise bending moments were applied to the 3D FE model, with which the deformed cross-section shapes were calculated. The new polars were determined with XFOIL and were fed into additional aero-servo-elastic simulations. Hence, five aero-servo-elastic simulations were carried out, one with undeformed cross-sections, and four with deformed cross-sections calculated from the bending moment distributions at the four azimuth positions mentioned above and highlighted in Fig. 5.

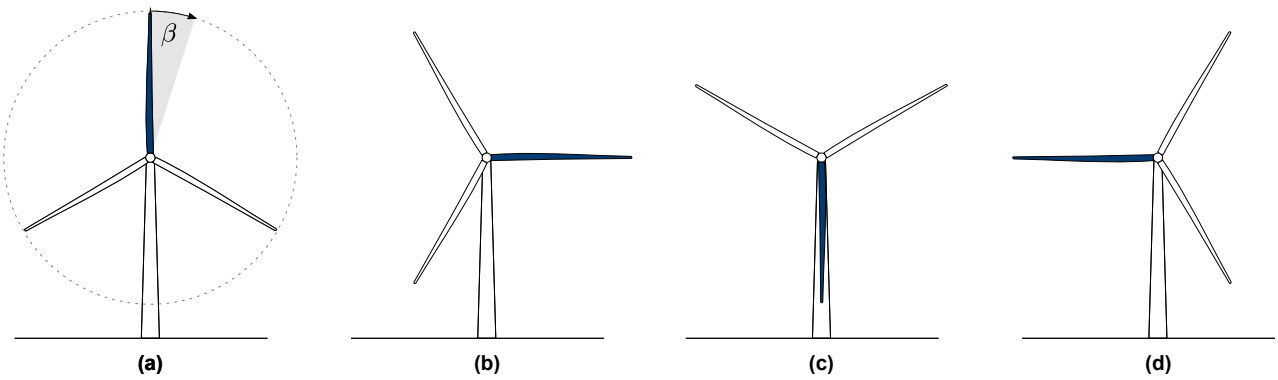

Figure 5. Wind turbine rotor positions considered in this study. The rotor blade loads are evaluated at four azimuth angles β indicated by the blue rotor blade, i. e., **(a)** $\beta = 0°$, **(b)** $\beta = 90°$, **(c)** $\beta = 180°$, and **(d)** $\beta = 270°$.

3 Cross-sectional deformations

In this section, the cross-sectional deformations at two exemplary positions along the blade are discussed.

Recall the blade element theory (Hau, 2013). Each rotor blade is divided into so-called blade elements. The lift and drag forces on blade element level, which are denoted by $\mathrm{d}F_\mathrm{L}$ and $\mathrm{d}F_\mathrm{D}$, can be calculated at steady-state conditions by the relations

$$\mathrm{d}F_\mathrm{L} = \frac{\rho}{2}\, c_\mathrm{L}(\alpha)\, u_\mathrm{rel}^2\, c\, \mathrm{d}r \quad \text{and} \quad \mathrm{d}F_\mathrm{D} = \frac{\rho}{2}\, c_\mathrm{D}(\alpha)\, u_\mathrm{rel}^2\, c\, \mathrm{d}r\,, \tag{2}$$

where ρ denotes the mass density of air, $c_\mathrm{L}(\alpha)$ and $c_\mathrm{D}(\alpha)$ are the lift and drag coefficients at a given angle of attack α, u_rel is the relative inflow velocity, c is the chord length, and $\mathrm{d}r$ is the radial extension of the blade element under consideration. The change in airfoil geometry due to deformation can affect the chord length c as well as the lift and drag coefficients and therefore have an impact on the lift and drag forces.

3.1 Change in airfoil shape

The internal loads at the four rotor positions (blade at 3, 6, 9 and 12 o'clock) were extracted. These bending moments were transformed into the global blade coordinate system, which was required for the 3D FE simulations. The resulting bending moments are shown together with the blade positions and the cross-sectional deformations in Fig. 6. The dashed lines represent the flapwise bending moment while the dash-dotted lines the edgewise bending moment, respectively. In each blade position the absolute values of the bending moments are highest at the blade root and continuously decrease to zero at the blade tip.

Fig. 6 (a) shows the loads and cross-sectional deformation for the blade position of $\beta = 0°$ (12 o'clock). The rotor blade points upwards, so that its weight has a negligible effect on the bending moments. Both the flapwise and the edgewise bending moments have a positive sign. This means that the blade bends towards the suction side and towards the leading edge. The maximum flapwise bending moment is approximately 10.6 times bigger than the maximum edgewise bending moment.

As shown in Fig. 6 (b), the tip of the rotor blade points to the side at $\beta = 90°$ (3 o'clock), with the leading edge downwards. In this position, the weight of the blade has a major influence on the edgewise bending moment. Hence, the edgewise bending moment is bigger than at $\beta = 0°$. Since the wind field is constant, the flapwise bending moment remains almost the same. The maximum flapwise bending moment is still approximately 2.6 times bigger than the edgewise bending moment.

At a blade position of $\beta = 180°$ (6 o'clock), the rotor blade is vertically aligned and points downwards, see Fig. 6 (c). The bending moments are similar to those at a blade position of $\beta = 0°$, because the blade's weight is negligible and the bending moments are governed by aerodynamic forces.

At a blade position of $\beta = 270°$ (9 o'clock), the blade tip points to the side with the leading edge upwards, see Fig. 6 (d). The weight is now counteracting the circumferential aerodynamic forces, so that the edgewise bending moments become negative. The absolute values of the flapwise bending moment at the blade root is 5.3 times bigger compared to the edgewise bending moment.

The bending moments were each applied to the 3D FE blade model. The deformed 2D cross-sections were extracted from the resulting deformed rotor blade. For the four blade positions, two cross-sections were exemplarily chosen for investigating the cross-sectional deformations in detail. Cross-section A is close to the maximum chord position at $(r/R)_\mathrm{A} = 0.21$ and cross-section B in the outboard region of the blade at $(r/R)_\mathrm{B} = 0.75$. The cross-sectional deformations of these two cross-sections are shown on the right-hand side of Fig. 6. For visualisation purposes, the chord lengths of the cross-sections are normalized and the deformation vectors are magnified by a scaling factor of 5. The shear webs are not shown, since they are not important for the aerodynamic forces. The black lines show the undeformed geometries of the cross-sections, while the red lines show the deformed cross-sections. In between, arrows are used to highlight the deflection vectors.

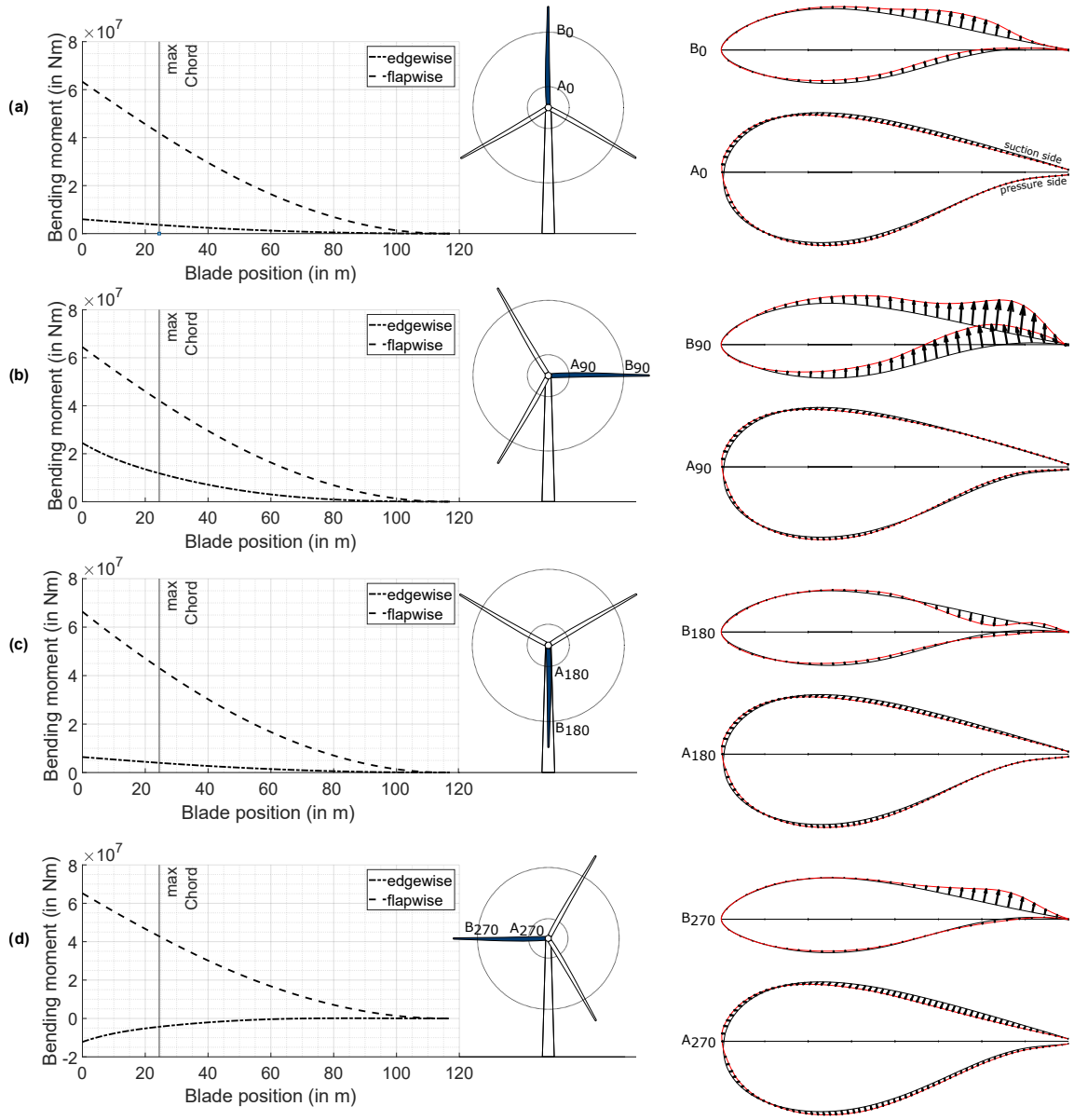

Figure 6. Bending moment distributions and cross-sectional deformations at two positions along the rotor blade for four different azimuth positions of the blade. The rotor positions are $(r/R)_{\mathrm{A}} = 0.21$ and $(r/R)_{\mathrm{B}} = 0.75$. The azimuth positions are **(a)** $\beta = 0°$ (12 o'clock), **(b)** $\beta = 90°$ (3 o'clock), **(c)** $\beta = 180°$ (6 o'clock), and **(d)** $\beta = 270°$ (9 o'clock).

For the cross-section A at $\beta = 0°$ (denoted by A_0), small deformations are detectable. On the suction side between the trailing edge and approximately $c/4$, the shell deforms into the cross-section. From approximately $c/4$ up to the leading edge, the suction side shell deforms out of the cross-section. From the leading edge up to approximately $c/8$, the shell on the pressure side deforms into the cross-section. From there on up to approximately $5c/8$, the pressure side shell deforms out of the cross-section. After this point up to the trailing edge, the pressure side shell hardly deforms, neither out of nor into the cross-section. The deformation of cross-section A at $\beta = 180°$ (denoted by A_{180}) looks very similar, because the load distribution is very similar. At $\beta = 90°$, the trailing edge of cross-section A (denoted by A_{90}) rotates slightly clockwise, i. e., the deformation into the cross-section on the suction side vanishes and the zero deformation on the pressure side changes to a deformation into the cross-section. The deformation in the rest of the cross-section is very similar to A_0 and A_{180}. At $\beta = 270°$, the trailing edge slightly rotates counter-clockwise, i. e., there is a deformation into the cross-section on the suction side and a deformation out of the cross-section on the pressure side.

The sign of the edgewise bending moment is a major difference in loading between A_{90} and A_{270}, and the magnitude of the edgewise bending moment is changing significantly during one rotation. Contrarily, the flapwise bending moment is almost constant. The deformation in the vicinity of the trailing edge changes with the rotation, but in the other regions of the cross-section the deformation is constant. Hence, the deformation in the vicinity of the trailing edge seems to be governed by the edgewise bending moment (rotation of the trailing edge clockwise for positive edgewise bending moments and rotation of the trailing edge counter-clockwise for negative edgewise bending moments). The rest of the deformation is similar in all positions and is thus dominated by flapwise bending.

The cross-section B does not show any deformation around the leading edge at all four positions of the blade. At $\beta = 0°$ (denoted by B_0), the deformation at the trailing edge is also almost zero. However, in the trailing edge shell of the suction side, there is a significant deformation out of the cross-section, and on the pressure side into the cross-section in a long region between the shear webs and the trailing edge. The deformation at $\beta = 90°$ (denoted by B_{90}) shows an additional rotation clockwise, which is similar to the findings in cross-section A. Hence, the deformation out of the cross-section on the suction side and into the cross-section on the pressure side are more pronounced compared to B_0. At $\beta = 180°$ (denoted by B_{180}), the deformation shows a clear difference compared to B_0. It appears as if there was a buckle into the cross-section close to the trailing edge on the suction side and a small buckle out of the cross-section on the pressure side. The deformation at $\beta = 270°$ (denoted by B_{270}) looks qualitatively similar to B_{90}, but the amplitude is much smaller. The dependencies between the cross-sectional deformations and the loading situations associated with the blade positions are not as clear for cross-section B as for cross-section A.

The cross-sectional deformations were determined for all cross-sections along the blade. However, due to space limitations, they cannot be discussed in detail here. Nevertheless, the changes in chord length and in lift and drag coefficients are presented in the following for all cross-sections.

3.2 Change in chord length

In addition to the actual change in geometry, a change in chord length was also observed. The chord length is defined as the distance between leading and trailing edge and was computed for the deformed cross-sections. The deviation between the chord length of the undeformed and the deformed cross-sections are plotted in Fig. 7. Each graph represents one blade position. The relative deviation is plotted against the normalised spanwise coordinate r/R, where r is the actual spanwise position and R is the spanwise position of the blade tip.

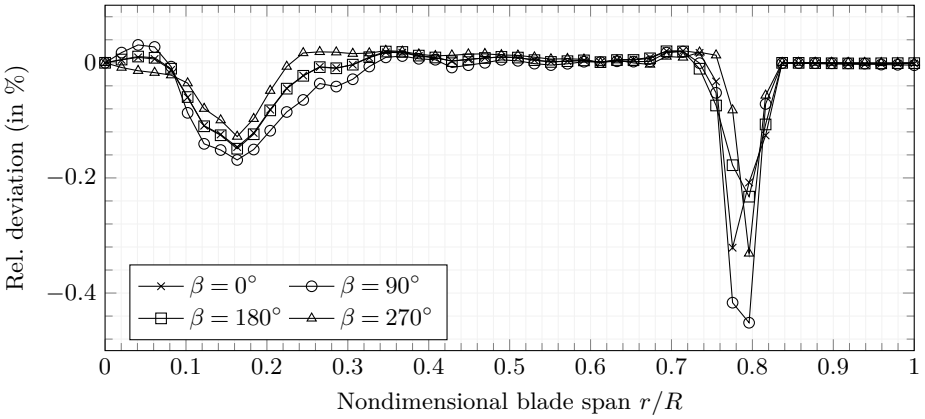

Figure 7. Relative deviation of the chord length between the deformed and the undeformed cross-section, plotted as a function of the normalised spanwise position along the blade.

The relative deviations of the chord length show a similar behavior for all four blade positions. There are two regions along the blade with a significant decrease in chord length. The first one is below 30 % of the blade length with a maximum chord length decrease of -0.16 %. This part of the blade also includes the maximum chord length and is subjected to the highest bending moments. The second portion with even higher relative deviation up to -0.45 % is beyond 70 % blade length up to the point where the last load frame is located. Because there is no load frame beyond 82 % blade length, no bending moments occur in this portion of the blade in the numerical model and consequently no deformations of the cross-sections. The radial portions between 30 % and 70 % blade length show a negligible amount of chord length deviation for the investigated load cases. The spanwise positions up to 10 % blade length is not evaluated here, because of multiple reasons. First, the deformations of the numerical model are not representative due to the fixed boundary conditions at the blade root. Second, the aerodynamic coefficients of the airfoils used in this section of the blade can not be evaluated with XFOIL, because of too high relative thicknesses. Due to the low radius and the low relative inflow velocity, this area of the blade has only a very small to negligible contribution to the aerodynamic performance and the aerodynamic loads of the blade, so that the error is considered negligible.

Based on the qualitative shape of the relative deviation of the chord length, we can derive where the cross-sections deformed the most. As the outer shell is the main factor in the calculation of the lift and drag coefficient, it can expected that the qualitative results will be similar.

3.3 Change in lift and drag coefficients

The deformed cross-sections were used to recalculate the aerodynamic performance of the blade in operation. Therefore, XFOIL simulations were conducted with the new cross-section geometries for the four blade positions. The results were included in the aero-servo-elastic simulations. Because time-dependent changes in airfoils cannot be modeled in OpenFAST, one simulation was conducted for each load scenario of the four blade positions using the same deformation for the entire rotor. The four simulations were then evaluated only at the rotor blade position corresponding to the position where the load was extracted. The lift and drag coefficients, each plotted against the normalised spanwise position along the blade for the four blade azimuth positions, are presented on the left-hand side of Fig. 8. Qualitatively, the distributions of the coefficients is similar for all blade positions. Quantitatively, there is a general slight difference in lift coefficients depending on the blade position. The quantitative difference in drag coefficients is not significant. In spanwise regions close to the root and close to $r/R = 0.8$, there are irregularities in the aerodynamic coefficients, especially in lift. These are associated with more significant and local cross-sectional deformations in these regions, see also section 3.2.

Note that the angle of attack also changes with different rotor positions due to the tilt and cone angles in the rotor and the associated vertically inclined inflow. Hence, we need to look at the relative deviations in lift and drag coefficients, which are shown on the right-hand side of Fig. 8. The relative deviation is calculated according to Eq. 1, with the undeformed blade simulation as the reference and the corresponding rotor position simulation as the generated value. Two regions along the blade span can be identified that show a change in aerodynamic properties. The first region is at around 20 % of the span, the second at around 80 % of the blade span. These were also the regions with the most significant changes in airfoil shape and chord length due to the cross-sectional deformations. A possible explanation is that 20 % blade span corresponds approximately with the region of maximum chord length. There, the trailing edge panels are the longest panels without stiffeners (shear webs) in the blade. Hence, small relative changes have a big absolute impact. Even though the relative deviation in lift coefficient is the highest here with 146 %, this region close to the blade root does not play a major role for the aerodynamic performance. The deviation close to the tip is likely linked to a lack of stiffness in this area, which is due to the fact that the blade is not in the final design stage, see Gaertner et al. (2020).

Overall, it can be seen when comparing Fig. 8 (b) and 8 (d) that the cross-sectioal deformation leads less to a loss in lift-coefficient and more to an increase in the drag coefficient. This is consistent with the literature (recall Sec. 1). The relative deviation in the drag coefficient allows the assumption that the resulting loads are greatest for $\beta = 180°$.

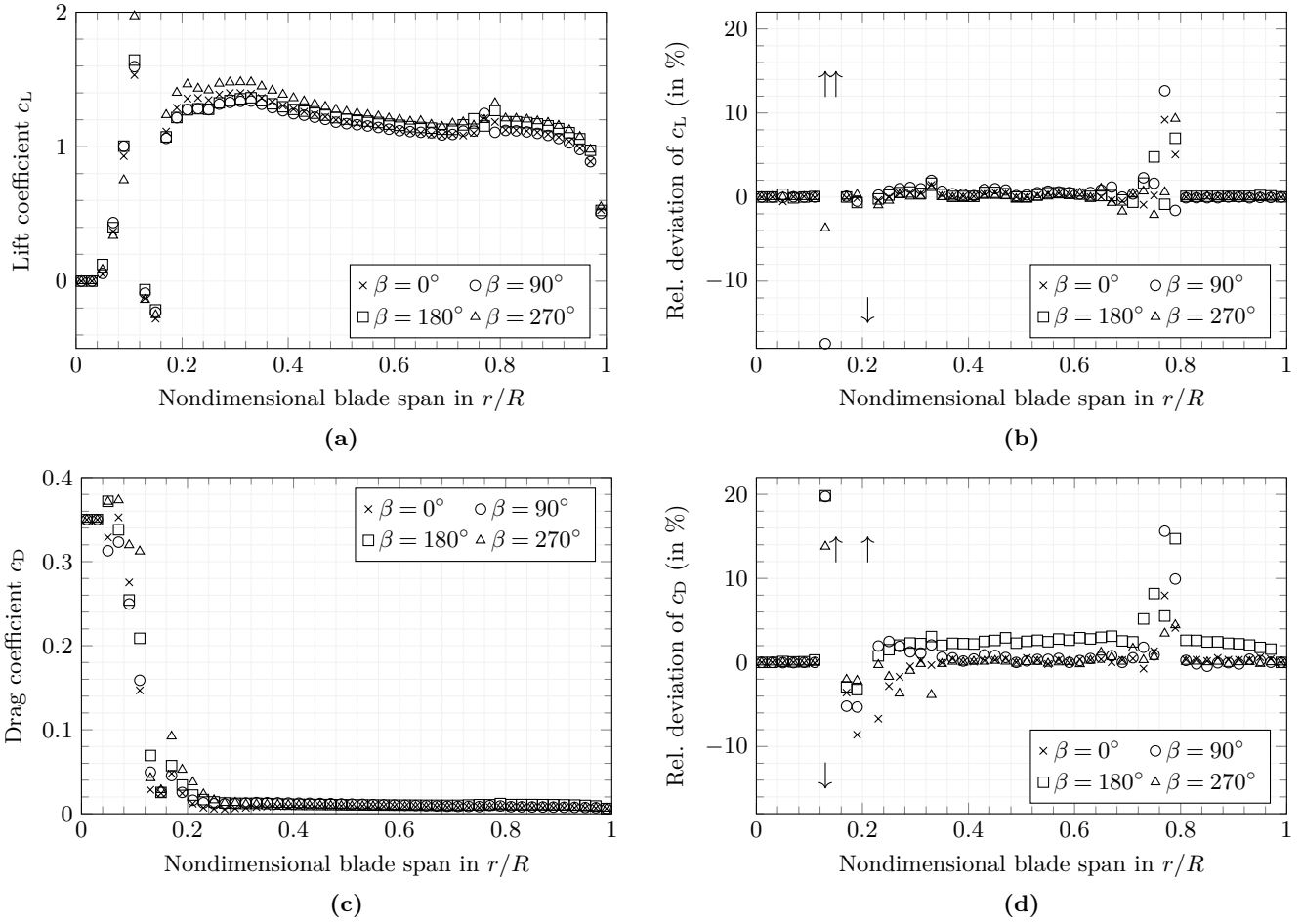

Figure 8. Comparison of the aerodynamic performance. The lift coefficient **(a)**, the relative deviation of the lift coefficient **(b)**, the drag coefficient **(c)** and the relative deviation of the drag coefficient **(d)** are plotted as functions of the normalised spanwise position along the blade for the four analysed azimuth positions of the blade. The values are taken from the respective OpenFAST simulations.

4 Coupling effect on the turbine behaviour

The aim of this section is to compare the wind turbine behaviour with and without the cross-sectional deformations of the blade. For the comparison, the chord length distribution and the aerodynamic coefficients were updated in the aero-servo-elastic simulations. For the cross-sectional deformations in each blade azimuth position, an OpenFAST
330 simulation was carried out in which the new aerodynamic parameters were used for all three blades. The in-plane and the out-of-plane blade root bending moments for one full rotation of the rotor will be analysed in the following.

The in-plane blade root bending moments are plotted in Fig. 9. The continuous black line represents the configuration with undeformed cross-sections. The values that are compared with those including the cross-sectional

deformations are highlighted by cross markers. Circular markers are used to show the blade root bending moments based on the cross-sectional deformations calculated for the respective azimuthal position of the blade. The deviations are relatively small. Hence, zoomed cutouts of the time series are plotted and the relative deviation ϵ was calculated. At azimuth positions of $\beta = 0°$ and $\beta = 180°$, the relative deviations are comparably high with $\epsilon = +1.1$ % and $\epsilon = -1.4$ %, respectively. They are at least one order of magnitude smaller at blade positions of $\beta = 90°$ and $\beta = 270°$ with $\epsilon = -0.16$ % and $\epsilon = +0.08$ %, respectively.

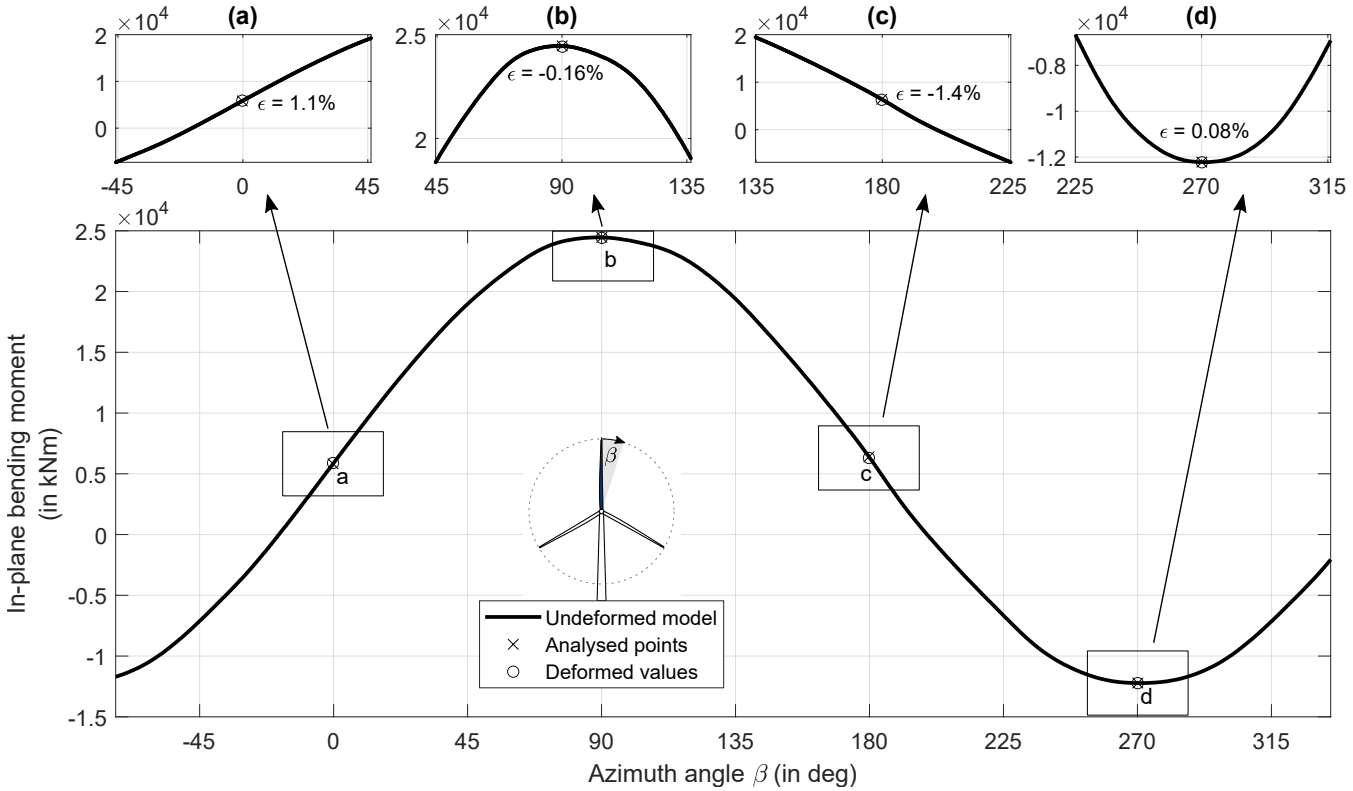

Figure 9. Comparison of the in-plane blade root bending moments. The turbine response with cross-sectional deformations in the four analysed azimuth positions is compared with the turbine response without cross-sectional deformations.

Due to the relative deviation in chord length, it was assumed that the loads would show the greatest deviation at $\beta = 90°$. However, it turns out that the greatest change occur at $\beta = 0°$ (+) and at $\beta = 180°$ (-). This also seems plausible, as the relative change in the drag coefficient is of higher magnitude than the change in chord length.

The out-of-plane blade root bending moments are plotted in Fig. 10. The relative deviation is in the same order of magnitude for all rotor positions and varies between $\epsilon = 0.32$ % at an azimuth position of $\beta = 270°$ and $\epsilon = 0.71$ % at $\beta = 90°$, i. e., in the horizontal blade positions. The relative deviations for the vertical blade positions is approximately the mean of the horizontal positions with $\epsilon = 0.57$ % at $\beta = 0°$ and $\epsilon = 0.48$ % at $\beta = 180°$.

Here, the maximum value shows for $\beta = 90°$. We can see here a similar trend between out-of-plane bending moment and chord length deviation. A correlation to lift and drag coefficient, however, can not be derived.

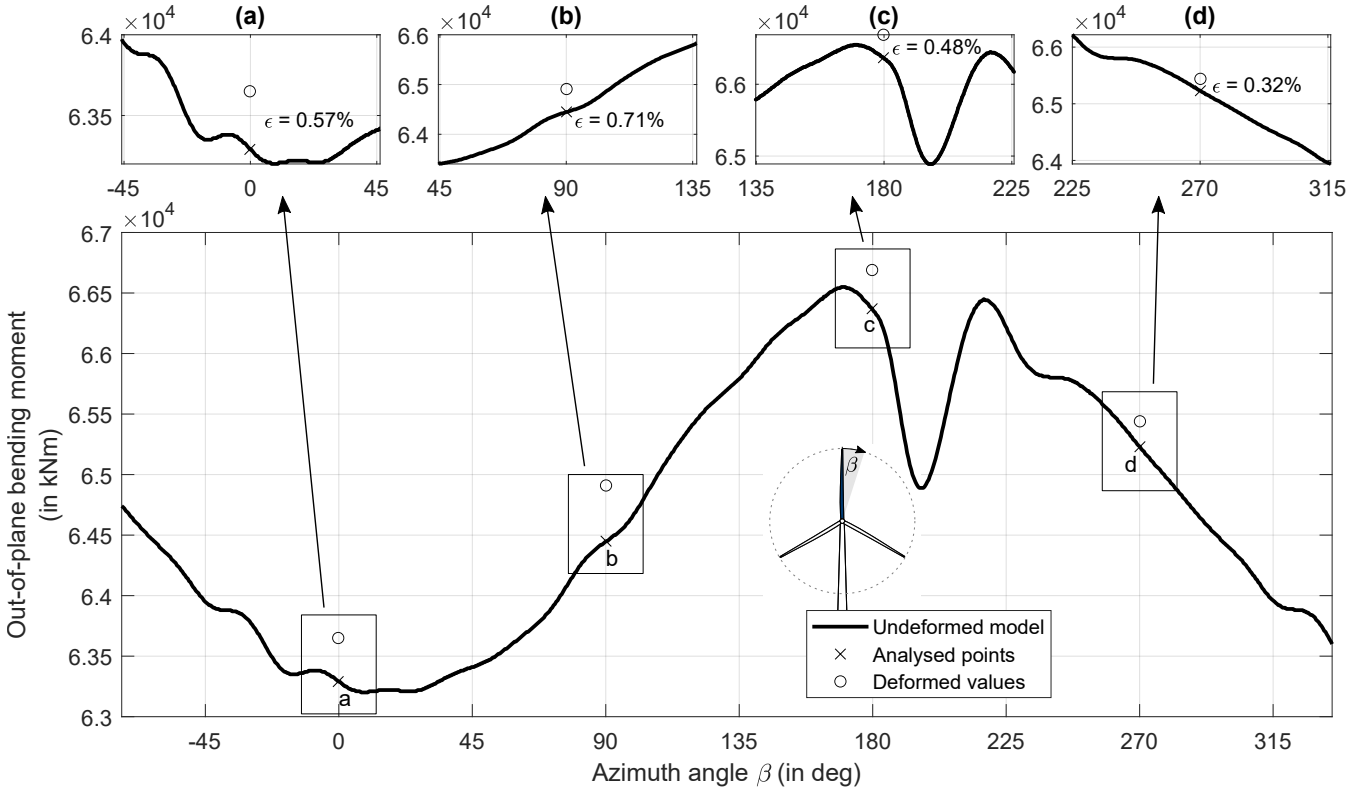

Figure 10. Comparison of the out-of-plane blade root bending moments. The turbine response with cross-sectional deformations in the four analysed azimuth positions is compared with the turbine response without cross-sectional deformations.

The impact of cross-sectional deformations on the in-plane bending moments is maximal for vertical blade positions. This is likely due to the asymmetries originating from the tilt and cone angles in the rotor, i. e., the vertically inclined inflow results in the highest relative inflow variations between the top and bottom vertical positions of the rotor. The cross-sectional deformations impact the chord lengths and the aerodynamic coefficients. As the aerodynamic forces and the corresponding bending moments scale quadratically with the relative inflow, it is natural that the vertical positions reveal the highest impact of cross-sectional deformations. Contrarily, the impact on the out-of-plane bending moments is maximal for the horizontal blade positions. This is natural, because edgewise bending is governed by gravitational forces that are activating maximum bending moments in horizontal positions of the blades.

This study revealed small changes in lift and drag coefficients, chord length as well as in-plane and out-of-plane bending moments. Even though the relative deviation of the bending moments is relatively small and potentially

within the uncertainty bandwidth of aero-servo-elastic simulations, the authors would like to emphasise the potential relevance of cross-sectional deformations for very large wind turbine blades. A variety of simplifications entered this initial investigation, i. e., no change in cross-sectional stiffnesses as a result of cross-sectional deformations, a simple load case with constant wind velocity at the rated wind speed, absence of dynamic effects from cross-sectional deformations (meaning an identical behaviour of all three rotor blades independent of their individual azimuth positions), and the use of the ElastoDyn module for the blades that does not account for torsion or higher bending modes. Even with the aforementioned simplified modeling approaches, small deviations regarding the bending moments at the blade root were observed. They are small, but non-zero and thus non-negligible. Reducing the amount of simplifications may increase the impact of cross-sectional deformations. A comparably low hanging fruit would be to use a BeamDyn model for the blades in order to more accurately describe the dynamic response of the blades including torsion. It is expected that especially torsion can result in significant in-plane cross-sectional deformations that were neglected in this study, but should be added in future work. Furthermore, other load cases such as ultimate load cases may result in load combinations that result in higher cross-sectional deformations. The trend to larger and increasingly slender blades may also result in more pronounced cross-sectional deformations in turbines exceeding a rated power of 20 MW or more. The aerodynamic analysis was carried out with a 2D panel method. However, it has not been investigated how the 3D deformation of the blade affects the aerodynamics. Such an investigation would involve a high computational effort, but it may be worth to investigate potential radial interactions of cross-sectional deformations. Moreover, the deformation of cross-sections in an operating wind turbine is a dynamic process. Hence, modeling this process dynamically may address other dynamic effects such as dynamic stall or dynamic wake, which would be interesting to study, especially in combination with more complex load cases including turbulence, pitch control, manoeuvres, etc.

5 Conclusions and outlook

This paper provides a first study analysing aero-elastic simulations of a wind turbine under consideration of cross-sectional deformations in the rotor blades. To the best knowledge of the authors, such investigation has not been carried out before by other groups.

The wind turbine model under investigation was the IEA 15 MW reference wind turbine. An initial simulation was carried out using aerodynamic coefficients (i.e. lift and drag coefficients) calculated with XFOIL. A simple load case was applied using a constant wind field at the rated wind speed. Four different bending moment distributions based on the azimuth angles of the blade were applied to a detailed 3D FE model of the rotor blade. The resulting cross-sectional deformations were analysed and used for a new calculation of lift and drag coefficients. Additionally, the change in chord lengths was computed and implemented in the aero-elastic turbine model. The deformations were especially present in the trailing edge panels. The change in chord length was identified in the vicinity of 20 % and 80 % of the blade span. This is also the range of blade span the load frames were applied. The cross-sections

with maximun chord length are in the area. Here, the relative deviation of chord length indicates a change in cross-sectional shape, which is in accordance with literature. The maximal deviation of chord length at 80 % might be a result from buckling. A more detailed analysis would be required for a precise statement. The relative deviation of the chord length in the deformed cross-sections compared with the chord length of the undeformed cross-sections was found to be below -0.45%. Four new OpenFAST simulations were performed including the new aerodynamic parameters as well as the new chord length distributions that were calculated for four different azimuth positions of the blade. The results show a maximum change in the blade root bending moments of -1.4 % for the in-plane bending moment and +0.71 % for the out-of plane bending moment.

These relative deviations are quite small. It needs to be highlighted that this only holds for an operational load case. This is based on the assumption that the cross-sectional deformations are greatest when the flapwise and edgewise bending moments are at their highest, i.e. rated wind speed. This leads to the conclusion that the aero-structural coupling between cross-sectional deformation and aerodynamic loads is negligible for operational loads.

However, it must be taken into consideration that a number of simplifications have been made. The torsional moment was not included in the calculation of cross-sectional deformations. For a more precise statement regarding cross-sectional deformations, torsion is planned to be included in the near future. Furthermore, the wind field was simplified using the rated wind speed and a constant wind field. The results show also with this assumptions a change. We therefore expect the influence on the aero-elastic simulation to be greater when analysing extreme load cases.

Appendix A: Comparison of FE model and IEA 15 MW reference turbine

Figure A1 shows selected geometrical (a)-(b) and structural (c)-(d) data as functions along the blade span for both the reference model and the FE model. The geometrical data comprise the chord length (top left) and the relative thickness (top right), the structural data the bending stiffnesses in the flapwise (out-of-plane bending, see Fig. A1 (c)) and the edgewise (in-plane bending, see Fig. A1 (d)) direction. For the MoCA model, the bending stiffnesses were calculated using BECAS (Blasques and Stolpe, 2012), which is a FEM tool that provides cross-sectional stiffness and mass matrices based on a 2D FE model and is widely used in the research community and the wind energy industry. The geometric parameters were chosen because they have a major influence on the aerodynamic behaviour of the rotor. The flapwise and edgewise stiffnesses were selected as structural representatives, because the investigations focus on the bending behaviour of the blades. In all subplots of Fig. A1, the data from the FE model is displayed by cross markers, that of the IEA 15 MW RWT model by circle markers.

Recall the definition of the relative deviation in Eq. (1). Figure A1 shows that the relative deviation of the chord length is below -0.1 %. This parameter is therefore considered to be accurately mapped. The relative thickness is also well represented in the FE model at spanwise positions where data points are given in the NREL data of the

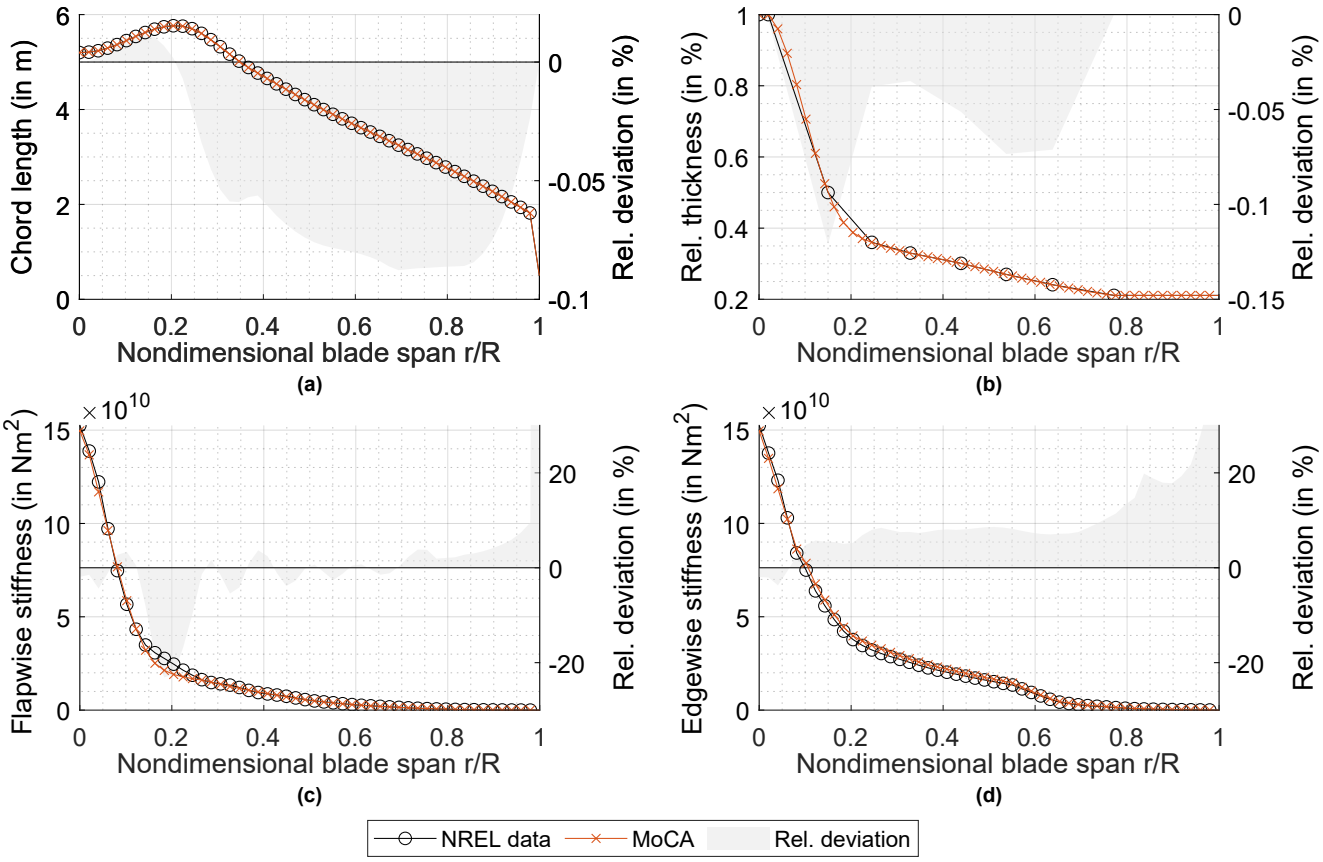

Figure A1. Comparison of the MoCA-based FE model and the IEA 15 MW reference turbine model. The chord length **(a)**, the relative thickness **(b)**, and the flapwise **(c)** and edgewise **(d)** stiffness are plotted as functions of the normalised blade span. The differences between the models are presented as relative deviation.

reference model (relative deviation below -0.12 %). However, in the reference model, the resolution of data points is relatively coarse, which are only given at the positions where the basic airfoils are defined. In the FE model, data points are also calculated equidistantly in between using piecewise cubic interpolation splines. Especially in the region where the geometry has large gradients, i. e., at spanwise positions of $r/R < 0.25$, this results in significant deviations compared to a linear interpolation in the reference model plotted in Fig. A1.

The flapwise and edgewise bending stiffnesses are plotted exemplarily together with the reference turbine data in Figs. A1 (c) and A1 (d). The stiffnesses generally agree very well. The deviation is largely less than -10 %. However, it can be seen that there is a significant deviation in the flapwise bending stiffness of up to -22 % in the range of the maximum chord length (around $r/R = 0.2$). This is due to the difference in relative thickness, which defines the distance between the spar caps and thus has a major impact on the flapwise bending stiffness. A significant difference in both the flapwise and the edgewise stiffnesses occurs at the blade tip due to a difference in chord length

at the tip. However, from a structural point of view, the blade tip is irrelevant, because the free end of the blade is unloaded. Moreover, the relative deviation increases towards the tip, because the absolute stiffness values decrease and approach zero towards the tip. The general small deviation of stiffnesses is likely due to differences in the tool chain to extract stiffnesses from a 3D model, where the processes of data calculation in the reference model is not absolutely clear.

Appendix B: Verification of airfoil polars between XFOIL and CFD

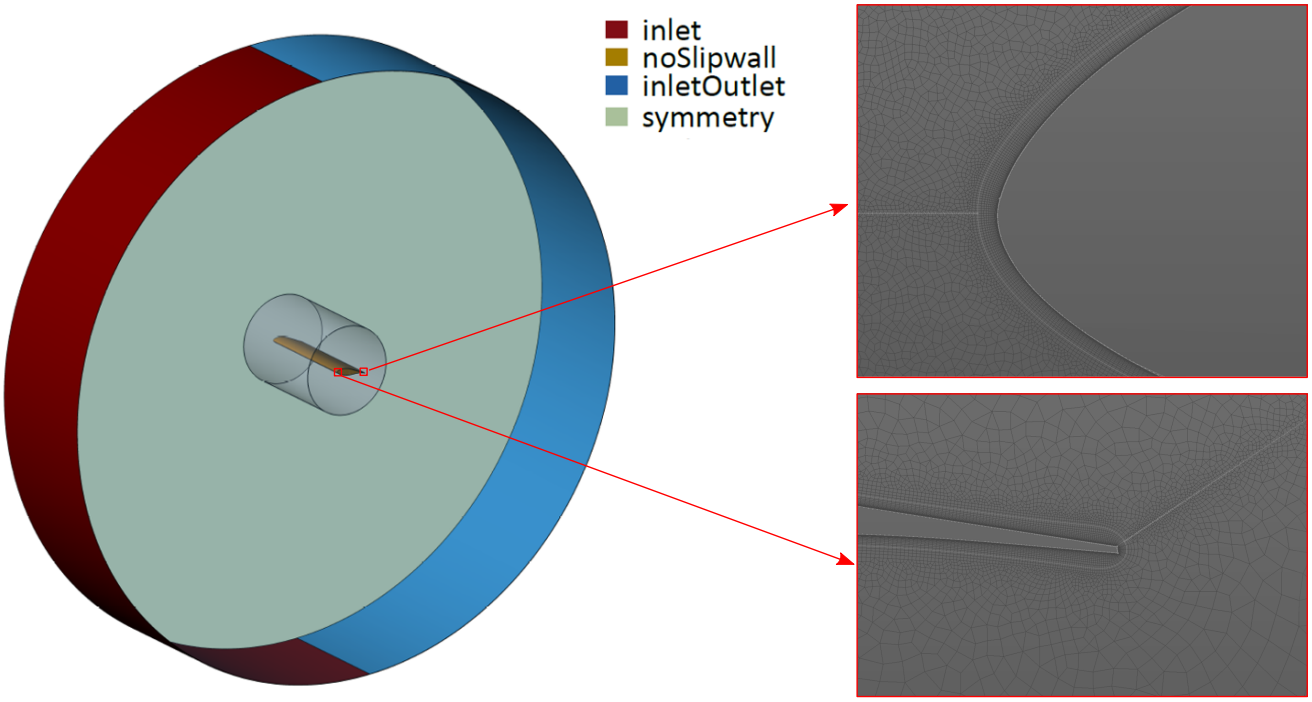

Figure B1. Boundary conditions and dimensions of the computational domain used to simulate the static polars with URANS.

Utilizing the open-source CFD solver OpenFOAM v2012, a three-dimensional transient Unsteady Reynolds-Averaged Navier-Stokes (URANS) simulation was conducted to determine the static polars of two selected deformed airfoils at spanwise positions of $(r/R)_{\mathrm{A}} = 0.21$ and $(r/R)_{\mathrm{B}} = 0.75$. The simulation was executed for a Reynolds number of $\mathrm{Re} = 3 \times 10^6$. The primary objective was to verify the lift and drag coefficients in the linear region of XFOIL. The computational domain, which is illustrated in Fig. B1, takes the form of a cylinder with a diameter of $50c$ and a length of $1c$ in the span-wise direction, where c is the chord length. These dimensions, previously employed by Yalcin et al. (2021), have proven effective in obtaining simulation results independent of far-field and spanwise mesh

Table B1. Initial and boundary conditions for the URANS simulations.

Boundary	$U_\infty, [\mathrm{m/s}]$	$p/\rho, [\mathrm{m^2/s^2}]$	$k, [\mathrm{m^2/s^2}]$	$\omega, [1/\mathrm{s^2}]$	$nut, [\mathrm{m^2/s}]$
Inlet	fixedValue, U_∞	zeroGradient	$I_\mathrm{t} = 0.05$	$L_\mathrm{mixing} = 0.2625$	calculated
Outlet	zeroGradient	fixedValue, 0	zeroGradient	zeroGradient	calculated
Airfoil	fixedValue, 0	zeroGradient	fixedValue, $1\mathrm{e}-9$	omegaWallFunction	nutlowReWallFunction
Walls [sides]	symmetry	symmetry	symmetry	symmetry	symmetry

Table B2. Numerical schemes for the URANS simulations.

Operator	Selected schemes	Accuracy order
ddtSchemes	backward	2^nd
gradSchemes (∇)	Gauss linear	2^nd
divSchemes ($\nabla\cdot$)	Gauss linearUpwind	2^nd upwind
laplacianSchemes (∇^2)	Gauss linear limited corrected, 0.5	2^nd

resolution. This allows for an in-depth analysis of flow phenomena around the airfoil. Boundary conditions for the computational domain are outlined in Tab. B1. Specifically, at the inlet, a uniform velocity and a zero gradient for kinematic pressure are applied, while at the outlet, a zero gradient for the velocity and a uniform kinematic pressure of $p/\rho = 0$ (indicating incompressible flow) are enforced. Wall boundaries adopt a symmetry condition, except for the airfoil surface where a zero-velocity condition prevails. Initial values for the internal fields are estimated using the inlet velocity, the hydraulic diameter, and the Turbulence Intensity (TI = 0.1%). The simulation employs the transient and incompressible pimpleFoam solver, incorporating the PIMPLE (merged PISO-SIMPLE) algorithm for pressure and velocity coupling (Issa, 1986). OpenFOAM utilizes the finite volume (fV) method to discretize differential terms in the RANS equation. The discretisation of the governing system of equations relies on a second-order finite volume approach in both space and time. Spatial discretisation employs a second-order upwind method as outlined by Warming and Beam (1976), while temporal discretisation follows the implicit three-point backward Euler scheme. Turbulence-related additional terms are modeled using the Shear Stress Transport (SST) approach, as introduced by Menter (1994). A summary of the applied numerical schemes can be found in Tab. B2.

Statistical convergence was monitored using the methodology introduced by Ries et al. (2018). The maximum ensemble error for all simulations was $1.8\mathrm{e}^{-2}$. The non-dimensional cell-height

$$y^+ = \frac{y \cdot \sqrt{\tau_\mathrm{w}/\rho}}{\nu} \approx 1 \tag{B1}$$

during all time steps, and $x^+_\mathrm{max} = 381$. These cell dimensions are sufficient to investigate integral blade loads for attached and separated flow (Ahrens et al., 2022).

Code and data availability. For legal reasons, code and data cannot be shared at this stage. The authors will try to provide code and data needed for reproduction of the findings by the time of final publication in case the manuscript will be accepted.

Author contributions. JG wrote the paper, did the literature research, implemented pre- and postprocessing scripts, carried out the simulations (except CFD), and prepared figures. FP contributed to the calculation of deformed cross-sections on the basis of 3D FE analyses and internally reviewed the paper. DA conducted CFD analyses and wrote the CFD part of section 2.2 and Appendix B. LW supervised DA and internally reviewed the paper. CB provided scientific guidance and supervision to JG in all project phases, internally reviewed the paper, and was responsible for funding acquisition.

Competing interests. The authors do not have competing interests.

Acknowledgements. The authors gratefully acknowledge the computing time granted by the Resource Allocation Board and provided on the supercomputer Lise and Emmy at NHR@ZIB and NHR@Göttingen as part of the NHR infrastructure. The calculations for this research were conducted with computing resources under the project nii00172. The research presented in this paper was funded by the Deutsche Forschungsgemeinschaft (DFG, Geman Research Foundation) as part of the Collaborative Research Center 1463 *Integrated Design and Operation Methodology for Offshore Megastructures* (SFB1463 – Project ID 434502799). The authors acknowledge the financial support.

References

Ahrens, J. D., Ziesse, M., Wein, L., and Seume, J. R.: A Novel And Costeffective Approach To Simulating Dynamic Stall On Rotating Wind Turbine Blades With A Changing Angle Of Attack, GPPS Chania, 2022.

Ansys®: Academic Research Mechanical APDL, Relase 2020 R2, 2020.

Bak, C.: Aerodynamic design of wind turbine rotors, in: Advances in wind turbine blade design and materials, pp. 79–128, Elsevier, 2023.

Balzani, C. and Gebauer, J.: Impact of shell structure stiffness on aero-structural coupling in wind turbine rotor blades, IOP Conf. Ser.: Mater. Sci. Eng., vol. 1293, p. 012025, https://doi.org/10.1088/1757-899X/1293/1/012025, 2023.

Blasques, J. P. and Stolpe, M.: Multi-material topology optimization of laminated composite beam cross sections, Composite Structures, 94, 3278–3289, 2012.

Brazier, L.: On the flexure of thin cylindrical shells and other" thin" sections, Proceedings of the Royal society of London. Series A, containing papers of a mathematical and physical character, 116, 104–114, 1927.

Burton, T., Jenkins, N., Bossanyi, E., Sharpe, D., and Graham, M.: Wind energy handbook, Wiley, 3 edn., ISBN 9781119451150, 2021.

Cecchini, L. S. and Weaver, P. M.: Brazier effect in multibay airfoil sections, AIAA journal, 43, 2252–2258, 2005.

Drela, M.: XFOIL: An Analysis and Design System for Low Reynolds Number Airfoils, in: Proceedings of the Conference, edited by Mueller, T. J., pp. 1–12, Springer Verlag, 1989.

Eder, M. A. and Bitsche, R.: A qualitative analytical investigation of geometrically nonlinear effects in wind turbine blade cross sections, Thin-Walled Structures, 93, 1–9, 2015a.

Eder, M. A. and Bitsche, R. D.: Fracture analysis of adhesive joints in wind turbine blades, Wind Energy, 18, 1007–1022, https://doi.org/10.1002/we.1744, 2015b.

Etemaddar, M., Hansen, M. O. L., and Moan, T.: Wind turbine aerodynamic response under atmospheric icing conditions, Wind Energy, 17, 241–265, 2014.

Gaertner, E., Rinker, J., Sethuraman, L., Zahle, F., Anderson, B., Barter, G., Abbas, N., Meng, F., Bortolotti, P., Skrzypinski, W., Scott, G., Feil, R., Bredmose, H., Dykes, K., Shields, M., Allen, C., and Viselli, A.: Definition of the IEA 15-Megawatt Offshore Reference Wind., Tech. Rep. NREL/TP-5000-75698, Golden, CO: National Renewable Energy Laboratory, 2020.

Gaudern, N.: A practical study of the aerodynamic impact of wind turbine blade leading edge erosion, in: Journal of Physics: Conference Series, vol. 524, p. 012031, IOP Publishing, 2014.

Gebauer, J. and Balzani, C.: Cross-Sectional Deformation of Wind Turbine Rotor Blades, in: International Ocean and Polar Engineering Conference, Ottawa, Canada, June 19-23, 2023, ISOPE-I-23-048.

Hansen, M. O. L.: Aerodynamics of wind turbines, Earthscan from Routledge, 3 edn., ISBN 9781315769981, 2015.

Haselbach, P. U., Eder, M. A., and Belloni, F.: A comprehensive investigation of trailing edge damage in a wind turbine rotor blade, Wind Energy, 19, 1871–1888, https://doi.org/10.1002/we.1956, 2016.

Hau, E.: Wind turbines: fundamentals, technologies, application, economics, Springer, 3 edn., ISBN 9783642271519, 2013.

Hodges, D. H.: Nonlinear composite beam theory, American Institute of Aeronautics and Astronautics, 2006.

IEC61400-23: Wind turbine generator systems - Part 23: Full-scale structural testing of rotor blades, International Electrotechnical Commission, ed. 1, 2001.

Issa, R. I.: Solution of the implicitly discretised fluid flow equations by operator-splitting, Journal of computational physics, 62, 40–65, 1986.

Jensen, F., Weaver, P., Cecchini, L., Stang, H., and Nielsen, R.: The Brazier effect in wind turbine blades and its influence on design, Wind Energy, 15, 319–333, 2012.

Jonkman, J. M., Hayman, G., Jonkman, B., Damiani, R., and Murray, R.: AeroDyn v15 user's guide and theory manual, NREL Draft Report, 46, 2015.

Kim, T., Hansen, A. M., and Branner, K.: Development of an anisotropic beam finite element for composite wind turbine blades in multibody system, Renewable Energy, 59, 172–183, 2013.

Larsen, T. J. and Hansen, A. M.: How 2 HAWC2, the user's manual, https://tools.windenergy.dtu.dk/HAWC2/manual/, accessed: 2024-10-21, 2023.

Lennie, M., Pechlivanoglou, G., Marten, D., Nayeri, C. N., and Paschereit, O.: A review of wind turbine polar data and its effect on fatigue loads simulation accuracy, Turbo Expo: Power for Land, Sea, and Air, 56802, V009T46A018, 2015.

Liu, X., Lu, C., Liang, S., Godbole, A., and Chen, Y.: Vibration-induced aerodynamic loads on large horizontal axis wind turbine blades, Applied Energy, 185, 1109–1119, 2017.

Madsen, H. A., Larsen, T. J., Pirrung, G. R., Li, A., and Zahle, F.: Implementation of the blade element momentum model on a polar grid and its aeroelastic load impact, Wind Energy Science, 5, 1–27, 2020.

Menter, F. R.: Two-equation eddy-viscosity turbulence models for engineering applications, AIAA Journal, 32, 1598–1605, https://doi.org/10.2514/3.12149, 1994.

National Renewable Energy Laboratory: OpenFAST User Documentation, https://openfast.readthedocs.io/en/main/, accessed: 2023-12-19, 2023.

National Renewable Energy Laboratory: BeamDyn User Guide and Theory Manual, https://openfast.readthedocs.io/en/main/source/user/elastodyn/index.html, accessed: 2024-10-21, 2024a.

National Renewable Energy Laboratory: ElastoDyn Users Guide and Theory Manual, https://openfast.readthedocs.io/en/main/source/user/elastodyn/index.html, accessed: 2024-07-08, 2024b.

Noever-Castelos, P., Haller, B., and Balzani, C.: Validation of a modeling methodology for wind turbine rotor blades based on a full-scale blade test, Wind Energ. Sci., 7, 105–127, https://doi.org/10.5194/wes-7-105-2022, 2022.

Ries, F., Nishad, K., Dressler, L., Janicka, J., and Sadiki, A.: Evaluating large eddy simulation results based on error analysis, Theoretical and Computational Fluid Dynamics, 32, 733–752, 2018.

Rosemeier, M. and Saathoff, M.: Impact of manufacture-induced blade shape distortion on turbine loads and energy yield, in: Journal of Physics: Conference Series, vol. 1618, p. 052011, IOP Publishing, 2020.

Schürmann, H. et al.: Konstruieren mit Faser-Kunststoff-Verbunden, vol. 2, Springer, 2007.

Söker, H.: Loads on wind turbine blades, in: Advances in Wind Turbine Blade Design and Materials, pp. 55–78, Elsevier, 2013.

Vassilopoulos, A. P.: Fatigue life prediction of wind turbine blade composite materials, in: Advances in wind turbine blade design and materials, pp. 251–297, Elsevier, 2013.

Warming, R. F. and Beam, R. M.: Upwind Second-Order Difference Schemes and Applications in Aerodynamic Flows, AIAA Journal, 14, 1241–1249, https://doi.org/10.2514/3.61457, 1976.

Yalcin, O., Cengiz, K., Wein, L., Özyörük, Y., and Seume, J. R.: Transitional DDES Study over a Circular Cylinder and an Airfoil Profile, The 13th International ERCOFTAC symposium on engineering, turbulence, modelling and measurements, 2021.